

# Comparison of free-surface and rigid-lid finite element models of barotropic instabilities

Laurent White<sup>1,2,\*</sup>, Jean-Marie Beckers<sup>3</sup>, Eric Deleersnijder<sup>2,1</sup>, Vincent Legat<sup>1</sup>

<sup>1</sup> Centre for Systems Engineering and Applied Mechanics (CESAME),  
Université Catholique de Louvain. 4, Avenue Georges Lemaître. B-1348 Louvain-la-Neuve, Belgium.

<sup>2</sup> G. Lemaître Institute of Astronomy and Geophysics (ASTR),  
Université Catholique de Louvain. 2, chemin du Cyclotron. B-1348 Louvain-la-Neuve, Belgium.

<sup>3</sup> Geohydrodynamics and Environmental Research, Université de Liège  
Sart Tilman B-5, B-4000 Liège, Belgium.

*Submitted to Ocean Dynamics on June 9, 2005*

## Abstract

The existence of atmospheric and oceanic meanders can be explained by the instability of zonal currents with respect to wave disturbances of small amplitude. Most theoretical and numerical results – e.g., stability conditions, growth rates, wavenumber of fastest growing mode – have been obtained by considering rigid-lid formulations. Those eliminate the propagation of surface waves and permit to focus on processes that evolve more slowly without computing an extraneous variable. The main goal of this work is to appraise the finite element method in the way it represents barotropic instabilities. To that end, three different formulations are employed. The free-surface formulation solves the primitive shallow-water equations while the vorticity-stream function and velocity-pressure formulations resort to the rigid-lid approximation. We investigate the role of the free surface and the way it alters the growth rates obtained with rigid-lid models. In that respect, growth rates for all three formulations are compared for hyperbolic-tangent and piecewise linear shear flows. Structured and unstructured meshes are utilized. Finally, the investigation is extended to timescales that allow for instability meanders to unfold, permitting the formation of eddies.

*Keywords:* Barotropic instabilities; numerical modeling; finite element method; free-surface flow

## 1 Introduction

The existence of fluctuations in atmospheric and oceanic flow patterns may be attributed to the inherent instability of their dynamical states. Depending on which energy source feeds the growing perturbations, instabilities essentially fall into two categories. Instabilities are referred to as barotropic or baroclinic according to whether their energy is extracted from the basic flow available kinetic energy or available potential energy, respectively. The first energy source, available kinetic energy, resides in the horizontal shear of the flow. The second energy source, available potential energy, is found in the horizontal pressure gradient. The latter is associated with vertical shear in the flow, in compliance with geostrophic balance (Pedlosky, 1964). Most instabilities, though, owe their existence to energy transfers from both sources. These instabilities are referred to as mixed instabilities or combined barotropic and baroclinic instabilities (see e.g., Hart, 1974; Kuo, 1978).

---

\*Corresponding author. E-mail: lwhite@mema.ucl.ac.be, Tel: +32 10 47 23 57, Fax: +32 10 47 21 80

This paper concentrates on barotropic instabilities and their modeling using three different finite-element formulations. The study of barotropic shear flow instabilities dates back to Kuo (1949). Kuo took one step further from the classical Rayleigh stability problem by incorporating the effect of latitude variation in the Coriolis parameter, the  $\beta$ -effect, whereby necessary conditions for instabilities are altered as compared with those derived for flows on an  $f$ -plane. These necessary conditions can be found in Kuo (1973) and Cushman-Roisin (1994) and are recalled in the present paper. When a flow is unstable, the question that comes to mind is how fast perturbations grow. As growth rates are generally not derivable for arbitrary zonal currents – only bounds can be extracted (Pedlosky, 1979) –, many authors have investigated specific basic flows in the past with the aim of evaluating growth rates. The zonal currents generally considered serve as an idealization of observed oceanic and atmospheric patterns. In that respect, the hyperbolic-tangent profile has been used quite often. Michalke (1964) studied this profile on an  $f$ -plane (no  $\beta$ -effect) system while Dickinson and Clare (1973) and Kuo (1973) computed perturbations growth rate and phase speed dependent on wavenumber and a dimensionless  $\beta$  parameter. Another typical basic state is a jet-type velocity profile, usually represented by a cosine squared or hyperbolic-secant squared (Kuo, 1973, 1978; Killworth, 1980). Further idealization of the hyperbolic-tangent profile as a piecewise linear profile is of interest for two reasons. First, as shown in Cushman-Roisin (1994), an analytical solution exists for the growth rate on an  $f$ -plane. Second, it is more amenable to numerical resolution, insofar as the profile is exactly represented – i.e., there is no truncation error – by low-order polynomial interpolation.

In this work, both the hyperbolic-tangent profile and its linear simplification are employed to investigate the behavior of two rigid-lid finite-element formulations as well as a free-surface formulation. The rigid-lid formulations are the standard vorticity-stream function and velocity-pressure formulations. The free-surface formulation solves the primitive shallow-water equations. The main goal of this paper is to appraise the finite element method in the way it represents barotropic instabilities. To that end, we first compare all three methods within the scope of small perturbations so that linear stability analysis remains valid and, aside from intercomparison, a reference analytical solution exists. In particular, the influence of the free-surface is to be assessed, since all theoretical results have been derived for the rigid-lid vorticity - stream function formulation. We then extend the investigation to timescales that allow for nonlinear advective terms to play a more significant role, permitting the development of eddies. In that respect, the way advection is numerically treated is pivotal because the quest for numerical stability more often than not precludes the unfolding of physical instabilities.

The paper is organized as follows. Section 2 lays out the problem formulation known as the barotropic stability problem. In section 3, all three finite-element formulations are presented in detail. Section 4 introduces the basic flows that are employed for comparisons in section 5. Conclusion makes up section 6.

## 2 Problem formulation

Since we will limit ourselves to motions whose scale is on the order of a few hundreds kilometers, the problem can be formulated in a cartesian coordinate system rather than in a spherical system. That is, the so-called annulus approximation will be made (Pedlosky, 1964): the two-dimensional domain of interest is deemed zonally infinite while the meridional extension remains finite. The  $\beta$ -effect is retained and flow occurs over a flat bottom. The unboundedness of the domain in the zonal direction is tackled by imposing periodicity in that direction. This design choice is mostly dictated by numerical feasibility but hardly constrains our framework: the basic flows only vary non-periodically in the meridional direction and wavy disturbances are, by nature, periodic. To further set out the framework, we define the coordinates  $(x, y)$  to be positive eastward and northward, respectively, while  $(u, v)$  are the corresponding velocity components. The system is assumed to be devoid of viscosity and all frictional effects at the bottom and the surface are neglected. Lateral boundaries are impermeable.

## 2.1 Governing equations

The inviscid nonlinear shallow-water equations will be used to model the system:

$$\frac{\partial u}{\partial t} + \mathbf{u} \cdot \nabla u - fv = -g \frac{\partial \eta}{\partial x}, \quad (1)$$

$$\frac{\partial v}{\partial t} + \mathbf{u} \cdot \nabla v + fu = -g \frac{\partial \eta}{\partial y}, \quad (2)$$

$$\frac{\partial \eta}{\partial t} + \nabla \cdot (H\mathbf{u}) = 0, \quad (3)$$

where  $\eta$  is the free-surface elevation with respect to an undisturbed reference level,  $f$  is the Coriolis parameter and is linearized about a reference latitude so that  $f = f_0 + \beta_0 y$ ,  $g$  is the acceleration due to gravity and  $H(x, y, t) = h + \eta(x, y, t)$  is the total fluid layer thickness with  $h$  being the constant undisturbed fluid thickness. In most barotropic shallow-water models, it is generally assumed that  $\eta \ll h$  so that the divergence of the transport  $H\mathbf{u}$  in (3) can be linearized to become  $\nabla \cdot (H\mathbf{u}) \simeq h\nabla \cdot \mathbf{u}$ , assuming also that the depth  $h$  is constant, as indicated above. Letting  $L$  be a characteristic length scale, the nondimensional form of (1)-(3) is

$$\frac{\partial u}{\partial t} + \mathbf{u} \cdot \nabla u - (1 + \beta y)v = -\frac{\partial \eta}{\partial x}, \quad (4)$$

$$\frac{\partial v}{\partial t} + \mathbf{u} \cdot \nabla v + (1 + \beta y)u = -\frac{\partial \eta}{\partial y}, \quad (5)$$

$$\frac{\partial \eta}{\partial t} + \alpha^2 \nabla \cdot \mathbf{u} = 0, \quad (6)$$

where the velocity scale is  $U = Lf_0$ , the time scale is  $T = L/U$  and the elevation scale  $E = L^2 f_0^2 / g$  is defined so that the Coriolis force and the elevation gradient are both on the same order of magnitude. Finally,  $\alpha$  is the ratio of the external deformation radius to the length scale

$$\alpha = \frac{\sqrt{hg}}{Lf_0}.$$

The dimensionless beta parameter is  $\beta = \beta_0 L^2 / U$ . Note that all variables are now dimensionless. Under typical oceanic shear flow conditions, we have  $\sqrt{hg} \simeq 10^2 \text{ m s}^{-1}$ ,  $L \simeq 10^4 - 10^5 \text{ m}$  and  $f_0 \simeq 10^{-5} - 10^{-4} \text{ s}^{-1}$  so that  $\alpha$  ranges from 10 to 1000 and  $\beta$  ranges from  $10^{-3}$  to  $10^{-1}$ . We see that under such conditions, a valid approximation to the continuity equation is that of a divergence-free velocity, also known as the rigid-lid approximation. Within that scope, (4)-(6) become

$$\frac{\partial u}{\partial t} + \mathbf{u} \cdot \nabla u - (1 + \beta y)v = -\frac{\partial p}{\partial x}, \quad (7)$$

$$\frac{\partial v}{\partial t} + \mathbf{u} \cdot \nabla v + (1 + \beta y)u = -\frac{\partial p}{\partial y}, \quad (8)$$

$$\nabla \cdot \mathbf{u} = 0, \quad (9)$$

where  $p$  is the pressure to be applied on top of the fluid layer to keep the surface flat and it has been nondimensionalized with a pressure scale  $P = \rho_0 L^2 f_0^2$ , where  $\rho_0$  is the fluid density. The continuity equation now acts as a constraint, effecting the velocity to be divergence-free. In that respect, the surface pressure is a diagnostic variable.

From (7)-(9), the vorticity-stream function formulation is derived by first defining the stream function  $\psi(x, y)$  so that  $u = -\frac{\partial \psi}{\partial y}$  and  $v = \frac{\partial \psi}{\partial x}$  while the relative vorticity  $\omega = \frac{\partial v}{\partial x} - \frac{\partial u}{\partial y} = \nabla^2 \psi$ . In so doing, the continuity equation is identically satisfied and both velocity components are derivable from a unique scalar variable – the stream function –, which permits to reduce the number of direct unknowns from three to one. The vorticity equation is obtained by computing  $\frac{\partial}{\partial x}(8) - \frac{\partial}{\partial y}(7)$ , which gives rise to

$$\frac{\partial \omega}{\partial t} + u \frac{\partial \omega}{\partial x} + v \frac{\partial \omega}{\partial y} = -\beta v.$$

Now, the two-equation system, whose vorticity equation is written in terms of the stream function, is

$$\frac{\partial \omega}{\partial t} - \frac{\partial \psi}{\partial y} \frac{\partial \omega}{\partial x} + \frac{\partial \psi}{\partial x} \frac{\partial \omega}{\partial y} = -\beta \frac{\partial \psi}{\partial x}, \quad (10)$$

$$\nabla^2 \psi = \omega. \quad (11)$$

Notice that this system could be collapsed onto a single equation for the stream function, without resorting to the substitution variable  $\omega$ . However, advective terms would then take on third-order spatial derivatives, which would require undesirable, high-order interpolants. Furthermore, using the relative vorticity permits to treat the nonlinear terms more easily as if  $\omega$  were simply be advected by the velocity field, derived from the stream function. We must bear in mind, though, that (10) is *not* a traditional advection equation, for the stream function depends on the vorticity. Hence, although it seems like we do away with the nonlinearity, it is concealed and entrenched within the problem. The stream function needs be specified at the southern and northern boundaries, where it has to be set to a constant that depends on the problem under consideration. It is also worth unveiling what looks like a paradox in (10). As far as the Coriolis term is concerned, only the  $\beta$ -effect remains. If only the  $f$ -plane approximation were made, the right-hand side of (10) would vanish and it would not be possible to say whether or not flow occurs within a rotating framework. In fact, any solution to (10) – with  $\beta = 0$  – in a rotating framework or in an inertial framework would be the same because both would obey the same equation. The vorticity equation (10) is identical to the one derived within the scope of the geostrophic approximation in Pedlosky (1979), where the author concludes that the sole effect of the earth’s sphericity on the geostrophic solution is due entirely to the variation of  $f$  with latitude but not on  $f$  itself.

Considering the rigid-lid approximation (7)-(9) again, another formulation can be had by taking the divergence of the momentum equations to derive a Poisson equation for the pressure. We first write the momentum equations (7)-(8) in vectorial form

$$\frac{\partial \mathbf{u}}{\partial t} + (\mathbf{u} \cdot \nabla) \mathbf{u} + \mathbf{F}^c = -\nabla p, \quad (12)$$

where  $\mathbf{F}^c = (1 + \beta y) \hat{e}_z \wedge \mathbf{u}$  is the Coriolis force, with  $\hat{e}_z$  being the upward-pointing unit vector. To derive the continuous pressure Poisson equation (PPE), we take the divergence of (12), giving rise to

$$-\nabla^2 p = \nabla \cdot [(\mathbf{u} \cdot \nabla) \mathbf{u}] + \nabla \cdot \mathbf{F}^c. \quad (13)$$

In deriving (13), the divergence and time differentiation have been interchanged so that use could be made of the continuity equation. The issue of Neumann pressure boundary conditions has been settled by Gresho and Sani (1987): take the normal projection of (12) onto  $\Gamma$ , namely

$$\frac{\partial p}{\partial n} = -\hat{\mathbf{n}} \cdot \mathbf{g} \quad \text{on } \Gamma, \quad (14)$$

where the condition  $\mathbf{u} \cdot \hat{\mathbf{n}} = 0$  on  $\Gamma$  was called on and where  $\mathbf{g}$  regroups the advection and Coriolis terms of (12). Note that  $\hat{\mathbf{n}}$  is the outward-pointing normal to the boundary. The pressure computed from (13) is known up to an arbitrary additive constant. To summarize, the velocity-pressure formulation is given by

$$\frac{\partial u}{\partial t} + \mathbf{u} \cdot \nabla u - (1 + \beta y)v = -\frac{\partial p}{\partial x}, \quad (15)$$

$$\frac{\partial v}{\partial t} + \mathbf{u} \cdot \nabla v + (1 + \beta y)u = -\frac{\partial p}{\partial y}, \quad (16)$$

$$-\nabla^2 p = \nabla \cdot [(\mathbf{u} \cdot \nabla) \mathbf{u}] + \nabla \cdot \mathbf{F}^c. \quad (17)$$

## 2.2 Linear stability analysis

Any given zonal shear flow  $(\bar{u}(y), 0)$  – henceforth called basic state – is solution to the *steady-state* nonlinear system of equations (4)-(6), provided that the elevation  $\bar{\eta}$  be in geostrophic equilibrium. In this case, the equations reduce to

$$(1 + \beta y)\bar{u}(y) = -\frac{d\bar{\eta}}{dy},$$

whereupon  $\eta(y)$  can be solved for, up to an arbitrary additive constant. Now, given such a basic flow  $(\bar{u}(y), 0, \bar{\eta}(y))$ , and beyond knowing whether it is stable or not, we are interested in the evolution of perturbations  $(u', v', \eta')$  of this basic state. We may recast the problem unknowns in terms of sums of (known) basic state variables and perturbations unknowns, the latter being much smaller in amplitude than the basic state variables. We thus rest within the realm of linear stability analysis insofar as all products of perturbation variables may safely be neglected. In so doing, we have

$$\begin{aligned} u(x, y, t) &= \bar{u}(y) + u'(x, y, t), \\ v(x, y, t) &= v'(x, y, t), \\ \eta(x, y, t) &= \bar{\eta}(y) + \eta'(x, y, t), \end{aligned}$$

and substituting these variables into (4)-(6) yields the following linearized evolution equations for the perturbations

$$\frac{\partial u'}{\partial t} + \bar{u} \frac{\partial u'}{\partial x} + v' \frac{d\bar{u}}{dy} - (1 + \beta y)v' = -\frac{\partial \eta'}{\partial x}, \quad (18)$$

$$\frac{\partial v'}{\partial t} + \bar{u} \frac{\partial v'}{\partial x} + (1 + \beta y)u' = -\frac{\partial \eta'}{\partial y}, \quad (19)$$

$$\frac{\partial \eta'}{\partial t} + \alpha^2 \frac{\partial u'}{\partial x} + \alpha^2 \frac{\partial v'}{\partial y} = 0. \quad (20)$$

Wavy disturbances in the  $x$ -direction are solutions to (18)-(20):

$$\begin{aligned} u'(x, y, t) &= U(y)e^{ik(x-ct)}, \\ v'(x, y, t) &= V(y)e^{ik(x-ct)}, \\ \eta'(x, y, t) &= H(y)e^{ik(x-ct)}. \end{aligned}$$

where  $k$  is the zonal wavenumber,  $c = c_r + ic_i$  is the complex phase speed and  $kc_i$  denotes the growth rate. Substituting these expressions into (18)-(20) yields the following coupled system of ordinary differential equations (ODEs) in  $U(y)$ ,  $V(y)$  and  $H(y)$ :

$$\begin{aligned} -kc U(y) + ik \bar{u} U(y) - (1 + \beta y)V(y) &= -ik H(y), \\ -kc V(y) + ik \bar{u} V(y) + (1 + \beta y)U(y) &= -\frac{dH}{dy}, \\ -kc H(y) + \alpha^2 ik U(y) + \alpha^2 \frac{dV}{dy} &= 0, \end{aligned}$$

to which the trivial solution  $U = V = H = 0$  is to be ruled out. In order to have instability, it is required that the disturbances grow exponentially in time. Deriving necessary (and sufficient) conditions for instability – in terms of the basic state and the flow parameters – is far from being tractable if we deal with the above system of ODEs, where  $\bar{u}(y)$  is itself a function of  $y$ . However, it is a very well-known problem for rigid-lid formulations (Pedlosky, 1979; Cushman-Roisin, 1994). In that case, the time derivative of the elevation disappears from the continuity equation (20) and the pressure gradient replaces the elevation gradient in the momentum equations (18) and (19). We are then free to define a perturbation stream function and the eigenvalue problem reduces to one that involves a single equation in the perturbation stream function,

$$\left( \frac{\partial}{\partial t} + \bar{u} \frac{\partial}{\partial x} \right) \nabla^2 \psi' + \left( \beta - \frac{d^2 \bar{u}}{dy^2} \right) \psi' = 0,$$

whose general solution is

$$\psi'(x, y, t) = \phi(y)e^{ik(x-ct)},$$

with  $u' = -\frac{\partial\psi'}{\partial y}$  and  $v' = \frac{\partial\psi'}{\partial x}$ . This leads to an ODE for  $\phi(y)$

$$\frac{d^2\phi}{dy^2} - k^2\phi + \frac{\beta - \frac{d^2\bar{u}}{dy^2}}{\bar{u} - c}\phi = 0. \quad (21)$$

Requiring that  $c_i > 0$  to have growing instabilities translates to necessary conditions on the basic state. Assuming the existence of parallel boundaries at  $y = y_1$  and  $y = y_2$ , where the perturbation stream function  $\psi'$  vanishes, integral properties may be established (Kuo, 1978; Cushman-Roisin, 1994). Multiplying (21) by the conjugate function  $\phi^*$  and integrating the result across the entire domain gives rise to

$$- \int_{y_1}^{y_2} \left( \left| \frac{d\phi}{dy} \right|^2 + \kappa^2 |\phi|^2 \right) dy + \int_{y_1}^{y_2} \frac{\beta - d^2\bar{u}/dy^2}{\bar{u} - c} |\phi|^2 dy = 0, \quad (22)$$

whose imaginary part is

$$c_i \int_{y_1}^{y_2} \left( \beta - \frac{d^2\bar{u}}{dy^2} \right) \frac{|\phi|^2}{|\bar{u} - c|^2} dy = 0. \quad (23)$$

Therefore, requiring that  $c_i > 0$  implies that the integrand of (23) must change sign. This leads to the first necessary condition for instability, namely that the expression  $\beta - d^2\bar{u}/dy^2$  must vanish within the domain. Considering the real part of (22), we get

$$\int_{y_1}^{y_2} (\bar{u} - c_r) \left( \beta - \frac{d^2\bar{u}}{dy^2} \right) \frac{|\phi|^2}{|\bar{u} - c|^2} dy = \int_{y_1}^{y_2} \left( \left| \frac{d\phi}{dy} \right|^2 + \kappa^2 |\phi|^2 \right) dy. \quad (24)$$

Now, if the flow is unstable, the integral in (23) vanishes so that we may multiply it by  $(c_r - \bar{u}_0)$ , for any real constant  $\bar{u}_0$ , and add the result to (24) to obtain

$$\int_{y_1}^{y_2} (\bar{u} - \bar{u}_0) \left( \beta - \frac{d^2\bar{u}}{dy^2} \right) \frac{|\phi|^2}{|\bar{u} - c|^2} dy > 0, \quad (25)$$

which is equivalent to demanding that the expression

$$(\bar{u} - \bar{u}_0) \left( \beta - \frac{d^2\bar{u}}{dy^2} \right)$$

be positive in some finite portion of the domain. Hence, for the flow to be unstable, the following criteria must be met:

1.  $\beta - \frac{d^2\bar{u}}{dy^2}$  must vanish at least once within the domain,
2.  $(\bar{u} - \bar{u}_0) \left( \beta - \frac{d^2\bar{u}}{dy^2} \right)$  must be positive in at least some finite portion of the domain.

In the second condition,  $\bar{u}_0$  is the value of  $\bar{u}(y)$  where the expression of the first condition vanishes because it must be true for any real constant.

The problem we wish to solve may be stated as follows: *given an unstable basic state and a disturbance of given wavenumber  $k$ , track the evolution of the disturbance and evaluate its growth rate  $kc_i$ .* Two benchmark shear flows, whose unstable modes have been studied in the past (Dickinson and Clare, 1973; Kuo, 1978; Cushman-Roisin, 1994), will be presented and will serve as comparative tools between the three finite element formulations that are outlined below.

### 3 Three finite element models

We now proceed with the presentation of three different manners of wielding the problem laid out in the foregoing section. The first finite element formulation deals with the free-surface elevation as a prognostic variable while the last two assume that a rigid lid is applied onto the top of the fluid layer. The three formulations follow the same order as that used to introduce the equations in Section 2. That is, we present the free-surface, vorticity-stream function and velocity-pressure formulations, in that order. Even though for large-scale barotropic systems, the difference between free-surface and rigid-lid flows is marginal, as we will see, the differences between the corresponding finite element formulations are quite striking and prone to comparative analysis. Ironically, the formulations that are analytically more obedient – the rigid-lid formulations – bring about numerical challenges. Our objective in this work is definitely not to offer an overview of existing finite element formulations for the incompressible Navier-Stokes equations (see e.g., Gresho and Sani, 1998), but we thought it would be interesting to linger on two common formulations, not the least because the Coriolis term does not appear in the classical Navier-Stokes equations considered by Gresho and Sani and because the computation of the pressure sometimes remains subject to difficulties.

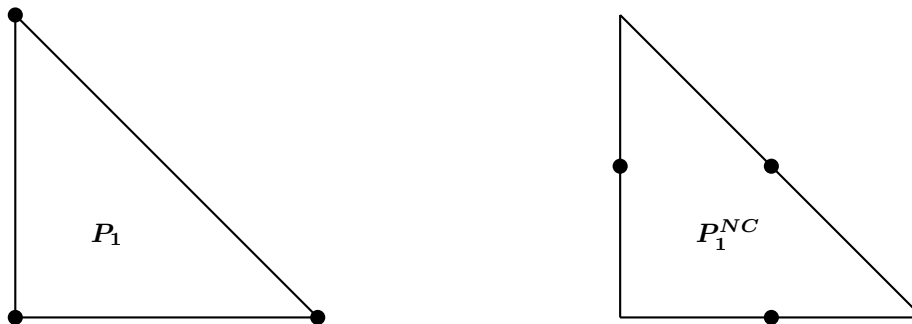


**Figure 1:** Nodes location for the  $P_1$  and  $P_1^{NC}$  discretizations.

Because we essentially have to solve an initial-value problem, and because disturbances might not grow as fast as one expect them to, all formulations presented below must be able to preserve a geostrophic equilibrium (given as initial state) with neither dissipation nor distortion, at least until roundoff errors kick in and destabilize the flow, if the latter is physically unstable. Any violation of this statement would render the associated formulation questionable, for any numerically-generated deviation – that is, not generated by forced disturbances – from this initial state would most likely falsify the analysis. Prior to presenting the finite element formulations, it is worth saying a few words about the elements that are used to approximate the various variables – the velocity, the pressure, the elevation, the vorticity and the stream function, depending upon which formulation is under scrutiny. Linear conforming and non-conforming elements will be used throughout the remainder of this section. As illustrated in Figure (1), the linear conforming element (the so-called  $P_1$  element) has its nodal values located at each vertex while the linear non-conforming element (the so-called  $P_1^{NC}$  element) has its nodal values located at the middle of each edge (see e.g., Hua and Thomasset, 1984; Hanert *et al.*, 2004). Their linear basis functions will be denoted by  $\phi_i^p$  and  $\phi_i^u$ , respectively, as a reminder that the pressure and elevation are conforming while the velocity is non-conforming. Conforming interpolation requires interpolated variables to be continuous across inter-element boundaries while non-conforming interpolation does not so; continuity is only ensured at the middle of each inter-element boundary. Finally, we abide by the following conventions: for a given mesh, it is assumed that there are  $M$  vertices

and  $N$  edges. A  $n$ -subscript indicates that the variable is time-discretized and evaluated at time  $t^n$ . The domain of interest is denoted by  $\Omega$  and its lateral boundary is noted  $\Gamma$ .

### 3.1 The free-surface formulation

Space-discretization of (4)-(6) is conducted by using the  $P_1^{NC}$  element for each velocity component and the  $P_1$  element for the elevation. Opting for the Galerkin finite element method, where test functions in the variational formulation are taken to be basis functions, the system (4)-(6) mutates to the following system of  $2N + M$  ordinary differential equations:

$$\mathbf{M}^u \frac{d\mathbf{R}}{dt} + \mathbf{A}\mathbf{R} + \mathbf{C}\mathbf{R} = -\mathbf{G}\mathbf{H}, \quad (26)$$

$$\mathbf{M}^p \frac{d\mathbf{H}}{dt} - \alpha^2 \mathbf{D}\mathbf{R} = 0. \quad (27)$$

In the above equations,  $\mathbf{M}^u$  is the non-conforming mass matrix,  $\mathbf{A}$  is the advection matrix,  $\mathbf{C}$  is the Coriolis matrix,  $\mathbf{G}$  is the gradient matrix and  $\mathbf{M}^p$  is the conforming mass matrix. The divergence matrix  $\mathbf{D}$  is obtained after integration by parts (the contour integral vanishes because  $\mathbf{u}_h \cdot \hat{\mathbf{n}} = 0$  on  $\Gamma$ , where  $\mathbf{u}_h$  is the discrete velocity field). Those matrices are written out below.

$$\begin{aligned} \mathbf{M}^u &= \begin{bmatrix} \langle \phi_i^u \phi_j^u \rangle & 0 \\ 0 & \langle \phi_i^u \phi_j^u \rangle \end{bmatrix} \in \mathbb{R}^{2N \times 2N}, \\ \mathbf{A} &= \begin{bmatrix} \langle \phi_i^u \mathbf{u}_h \cdot \nabla \phi_j^u \rangle & 0 \\ 0 & \langle \phi_i^u \mathbf{u}_h \cdot \nabla \phi_j^u \rangle \end{bmatrix} \in \mathbb{R}^{2N \times 2N}, \\ \mathbf{C} &= \begin{bmatrix} 0 & -\langle (1 + \beta y) \phi_i^u \phi_j^u \rangle \\ \langle (1 + \beta y) \phi_i^u \phi_j^u \rangle & 0 \end{bmatrix} \in \mathbb{R}^{2N \times 2N}, \\ \mathbf{G} &= \begin{bmatrix} \langle \phi_i^u \frac{\partial \phi_j^p}{\partial x} \rangle \\ \langle \phi_i^u \frac{\partial \phi_j^p}{\partial y} \rangle \end{bmatrix} \in \mathbb{R}^{2N \times M}, \\ \mathbf{D} &= \begin{bmatrix} \langle \frac{\partial \phi_i^p}{\partial x} \phi_j^u \rangle & \langle \frac{\partial \phi_i^p}{\partial y} \phi_j^u \rangle \end{bmatrix} \in \mathbb{R}^{M \times 2N}, \\ \mathbf{M}^p &= \begin{bmatrix} \langle \phi_i^p \phi_j^p \rangle \end{bmatrix} \in \mathbb{R}^{M \times M}, \end{aligned}$$

where  $\langle \rangle$  indicates integration over  $\Omega$ . It is conspicuous that the gradient matrix is the transpose of the divergence matrix, because integration by parts was carried out in the continuity equation. The classical treatment of the Navier-Stokes equations, though, usually implies integrating the pressure gradient by parts but not the divergence of the velocity, which leads to the same result whatsoever. Our choice is justified by the fact that we use non-conforming velocity elements. The vector  $\mathbf{R}$  contains the nodal values of both velocity components, that is

$$\mathbf{R} = \begin{bmatrix} \mathbf{U} \\ \mathbf{V} \end{bmatrix},$$

where  $\mathbf{U}$  and  $\mathbf{V}$  denote the nodal values of each velocity component. The vector  $\mathbf{H}$  contains the elevation nodal values. Note that the advection matrix  $\mathbf{A}$  depends upon the velocity, All three variables of the free-surface formulation – both components of the velocity and the elevation – are solved for in a coupled fashion. This allows for varying the degree of implicitness of the elevation gradient and the divergence of the velocity in the continuity equation. Time-discretization of (26) and (27) leads to

$$\begin{aligned} \mathbf{M}^u \frac{\mathbf{R}^{n+1} - \mathbf{R}^n}{\Delta t} + \mathbf{A}\mathbf{R}^n + \frac{1}{2}\mathbf{C}(\mathbf{R}^{n+1} + \mathbf{R}^n) &= -\mathbf{G} \left( \frac{1}{2}\mathbf{H}^{n+1} + \frac{1}{2}\mathbf{H}^n \right), \\ \mathbf{M}^p \frac{\mathbf{H}^{n+1} - \mathbf{H}^n}{\Delta t} - \alpha^2 \mathbf{D} \left( \frac{1}{2}\mathbf{R}^{n+1} + \frac{1}{2}\mathbf{R}^n \right) &= 0. \end{aligned}$$

Rearranging the above expressions so that all nodal values at time step  $t^{n+1}$  appear in the left-hand side while all nodal values at time step  $t^n$  appear in the right-hand side, we arrive at

the following coupled linear system in the  $2N + M$  nodal values:

$$\begin{cases} \left( \frac{\mathbf{M}^u}{\Delta t} + \frac{1}{2}\mathbf{C} \right) \mathbf{R}^{n+1} + \frac{1}{2}\mathbf{G}\mathbf{H}^{n+1} &= \left( \frac{\mathbf{M}^u}{\Delta t} - \mathbf{A} - \frac{1}{2}\mathbf{C} \right) \mathbf{R}^n - \frac{1}{2}\mathbf{G}\mathbf{H}^n, \\ -\frac{1}{2}\alpha^2\mathbf{D}\mathbf{R}^{n+1} + \frac{\mathbf{M}^p}{\Delta t}\mathbf{H}^{n+1} &= \frac{1}{2}\alpha^2\mathbf{D}\mathbf{R}^n + \frac{\mathbf{M}^p}{\Delta t}\mathbf{H}^n. \end{cases} \quad (28)$$

The Coriolis term is always treated semi-implicitly so as to not artificially generate nor dissipate energy, complying with the fact that the Coriolis force does not physically work. The free-surface formulation allows for the propagation of fast surface waves (e.g., Poincaré waves) whose phase speed is on the order of  $\sqrt{gh}$  and can therefore reach up to hundreds of  $\text{m s}^{-1}$ . If an explicit, forward-backward time scheme is used (Beckers and Deleersnijder, 1993), the CFL condition imposes too stringent of a time step, as compared with climatic timescales (see e.g., White, 2004). A semi-implicit treatment of the terms governing the propagation of those surface waves relaxes the constraint on the time step – the scheme becomes unconditionally stable – and serves the purpose of modeling large-scale features without resolving fast-propagating smaller-scale features. There is nevertheless a cost to unconditional stability: the system (28) is fully coupled and all variables must be solved for together. Note that advection is explicit. An alternative consists in treating the advected field implicitly while the advecting field remains explicit, which imposes the reconstruction of the full system left-hand side at each time step. Another alternative is to treat both the advecting and advected fields implicitly, a method that implies solving a nonlinear system at each time step. Both these alternatives are computationally expensive and are not considered in this paper.

### 3.2 The vorticity - stream function formulation

Both the vorticity and the stream function are discretized using the  $P_1$  element so that (10)-(11) is converted to the following system of  $2M$  ordinary differential equations

$$\mathbf{M}^p \frac{d\mathbf{W}}{dt} + \mathbf{N}\mathbf{W} = \mathbf{B}_\omega, \quad (29)$$

$$\mathbf{L}\mathbf{S} = \mathbf{B}_\psi, \quad (30)$$

where  $\mathbf{W}$  and  $\mathbf{S}$  are vectors of vorticity and stream function nodal values, respectively. The matrices  $\mathbf{N}$  and  $\mathbf{L}$  and the vectors  $\mathbf{B}_\omega$  and  $\mathbf{B}_\psi$  take on the following form:

$$\begin{aligned} \mathbf{N} &= \left[ \left\langle \phi_i^p \left( -\frac{\partial\psi_h}{\partial y} \frac{\partial\phi_j^p}{\partial x} + \frac{\partial\psi_h}{\partial x} \frac{\partial\phi_j^p}{\partial y} \right) \right\rangle \right] \in \mathbb{R}^{M \times M}, \\ \mathbf{L} &= \left[ \left\langle \nabla\phi_i^p \cdot \nabla\phi_j^p \right\rangle \right] \in \mathbb{R}^{M \times M}, \\ \mathbf{B}_\omega &= \left[ -\beta \left\langle \phi_i^p \frac{\partial\psi_h}{\partial x} \right\rangle \right] \in \mathbb{R}^M, \\ \mathbf{B}_\psi &= \left[ -\left\langle \phi_i^p \omega_h \right\rangle \right] \in \mathbb{R}^M, \end{aligned}$$

where  $\omega_h$  and  $\psi_h$  are the discrete vorticity and stream function fields. Note that the contour integral emanating from integration by parts of the Laplacian vanishes because only Dirichlet boundary conditions are enforced on  $\psi_h$ . Time-discretization of (29) yields

$$\mathbf{M}^p \frac{\mathbf{W}^{n+1} - \mathbf{W}^n}{\Delta t} + \frac{1}{2}\mathbf{N}\mathbf{W}^{n+1} + \frac{1}{2}\mathbf{N}\mathbf{W}^n = \mathbf{B}_\omega^n. \quad (31)$$

Rearranging (31), the full system is

$$\begin{cases} \mathbf{L}\mathbf{S}^n &= \mathbf{B}_\psi^n, \\ \left[ \frac{\mathbf{M}^p}{\Delta t} + \frac{1}{2}\mathbf{N} \right] \mathbf{W}^{n+1} &= \left[ \frac{\mathbf{M}^p}{\Delta t} - \frac{1}{2}\mathbf{N} \right] \mathbf{W}^n + \mathbf{B}_\omega^n, \end{cases} \quad (32)$$

and is set off by an initial condition on the vorticity. Notice that the advection matrix  $\mathbf{N}$  is always evaluated at time step  $t^n$  because decision was made to first solve for the stream function and then, for the new vorticity in terms of the stream function. In other words, the system is sequential in time. This procedure allows for a convenient way of handling the nonlinear advection term.

### 3.3 The velocity-pressure formulation

Discretization in space of (15)-(17) must be done carefully. A naive approach is to start with the continuous pressure Poisson equation (17) and discretize it. In so doing, the discretized Laplacian takes on the same expression as that obtained in the previous vorticity-stream function formulation. That is, the matrix  $\mathbf{L}$  is used to approximate  $-\nabla^2$ . This, however, yields an inconsistent – and unstable – discretization in the sense that the discrete pressure and velocity fields are incompatible with one another, for the velocity boundary conditions are not consistently incorporated within the discrete Laplacian operator. In fact, as shown in Gresho *et al.* (1984), the issue of deriving the discrete consistent pressure Poisson equation (PPE) must be addressed the other way around by working on the space-discretized form of the momentum and continuity equations to extract the discrete Laplacian operator. Both components of the velocity are discretized using the  $P_1^{NC}$  element while the pressure is interpolated with the  $P_1$  element. Space-discretization of (12), together with the continuity equation (9), lead to

$$\mathbf{M}^u \frac{d\mathbf{R}}{dt} + \mathbf{A}\mathbf{R} + \mathbf{C}\mathbf{R} = -\mathbf{G}\mathbf{P}, \quad (33)$$

$$\mathbf{D}\mathbf{R} = 0, \quad (34)$$

which consists of a system of  $2N$  ODEs in the nodal values  $\mathbf{R}$ , subject to the constraint that the velocity field be discretely divergence-free. All matrices and vectors used in this formulation were defined earlier when dealing with the free-surface formulation. We shall now proceed with the derivation of the so-called *consistent* PPE or CPPE. From (34), we may write

$$\mathbf{D} \frac{d\mathbf{R}}{dt} = 0,$$

and deduce that the discrete acceleration is divergence-free. Because the mass matrix  $\mathbf{M}^u$  is non-singular, we may isolate  $d\mathbf{R}/dt$  in (33) and substitute it into the newly-derived statement of divergence-free acceleration, leading to the following equation:

$$\mathbf{D} \frac{d\mathbf{R}}{dt} = \mathbf{D}\mathbf{M}^{u-1} (-\mathbf{A}\mathbf{R} - \mathbf{C}\mathbf{R} - \mathbf{G}\mathbf{P}),$$

whose left-hand side may be time-discretized, which, using the fact that we set the velocity at time step  $t^{n+1}$  to be discretely divergence-free, produces the following equation

$$-\frac{1}{\Delta t} \mathbf{D}\mathbf{R}^n = \mathbf{D}\mathbf{M}^{u-1} (-\mathbf{A}\mathbf{R}^n - \mathbf{C}\mathbf{R}^n - \mathbf{G}\mathbf{P}^n),$$

whereupon  $\mathbf{P}^n$  is to be solved for and is the discrete pressure corresponding to the discrete velocity field at time step  $t^n$ . Hence, the linear system is

$$\mathbf{D}\mathbf{M}^{u-1} \mathbf{G}\mathbf{P}^n = \mathbf{D}\mathbf{M}^{u-1} \left( \frac{1}{\Delta t} \mathbf{M}^u \mathbf{R}^n - \mathbf{A}\mathbf{R}^n - \mathbf{C}\mathbf{R}^n \right), \quad (35)$$

where  $-\nabla^2$  is now approximated by  $\mathbf{D}\mathbf{M}^{u-1} \mathbf{G}$ , which automatically incorporates the appropriate boundary conditions for the pressure (Gresho *et al.*, 1984). The previous expression loses its effectiveness if the matrix  $\mathbf{M}^u$  is not diagonal because  $\mathbf{M}^{u-1}$  will, in general, be dense. It is common practice to lump the mass when this occurs. This is where one of the key properties of the  $P_1^{NC}$  element comes into play: its basis functions are orthogonal to one another, which renders the matrix  $\mathbf{M}^u$  diagonal without having to resort to mass-lumping. Once the pressure

is known at time step  $t^n$ , we may march in time and use (33) to compute the velocity at the next time step. Time-discretization of (33), together with (35), yields the full consistent velocity-pressure formulation:

$$\begin{cases} \mathbf{D}\mathbf{M}^{u-1}\mathbf{G}\mathbf{P}^n & = \mathbf{D}\mathbf{M}^{u-1}\left(\frac{1}{\Delta t}\mathbf{M}^u\mathbf{R}^n - \mathbf{A}\mathbf{R}^n - \mathbf{C}\mathbf{R}^n\right), \\ \left(\frac{\mathbf{M}^u}{\Delta t} + \frac{1}{2}\mathbf{C}\right)\mathbf{R}^{n+1} & = \left(\frac{\mathbf{M}^u}{\Delta t} - \mathbf{A} - \frac{1}{2}\mathbf{C}\right)\mathbf{R}^n - \mathbf{G}\mathbf{P}^n. \end{cases} \quad (36)$$

The algorithm is started by specifying an initial velocity field, from which the initial pressure may be computed.

## 4 Two benchmark shear flows

The first basic state is a shear-zone type flow, consisting of two parallel and uniform currents on both sides of the shear layer, one oriented eastward and the other westward. Both currents have the same magnitude and the dimensionless analytical expression to represent this first basic state is

$$\bar{u}(y) = -\tanh(y), \quad (37)$$

The zonal flow (37) is represented on top panels of Figure (2). The second basic state is a piecewise linear function, whose expression is

$$\bar{u}(y) = \begin{cases} 1 & \text{if } y > 1 \\ y & \text{if } -1 < y < 1 \\ -1 & \text{if } y < -1 \end{cases} \quad (38)$$

and is featured on bottom panels of Figure (2). Panels on the left of Figure (2) show the meridional extent of the domain used in numerical experiments. In that particular case, the extension is 10 times larger than the shear layer width so as to emulate the absence of boundaries. Care will have to be taken to ensure sufficient mesh resolution within the shear layer. The basic flow (38) is less realistic than the hyperbolic-tangent (37) – the first derivative is discontinuous – but this simplification presents two advantages. First, an analytical expression for the dispersion relation of perturbations exists when the problem is formulated on an  $f$ -plane in a zonal channel of infinite width. Therefore, the growth rate of any wavelike disturbance of a given wavenumber is known. Second, because the profile is linear, it can be interpolated with low-order elements without any truncation errors. This ensures that no spurious surface waves propagate due to the inexact representation of the initial state. For such a profile, the issue of determining whether or not those spurious surface waves have an influence on the growth rate is obviated.

## 5 Numerical experiments

As already mentioned, any of the presented finite element formulations is to be ruled out, were it not able to preserve the unperturbed steady-state basic flow (in geostrophic equilibrium). The three methods, together with the *inconsistent* velocity-pressure formulation, are hereafter tested for their capacity in maintaining the steady state without artificial generation or dissipation of energy, nor distortion of the flow. It should be borne in mind that, since the free-surface formulation allows for the propagation of surface waves, distortion may occur but it ought to be energy-preserving. In Figure (3), the relative deviation of the total energy is shown for a 140-day run starting with an unperturbed hyperbolic-tangent basic flow. The mesh contains 8192 triangles and the time step is 2500 s. Whereas the rigid-lid vorticity-stream function formulation is energy-preserving (up to roundoff errors), the free-surface and consistent velocity-pressure formulations yield coinciding curves and feature maximum deviations of about 0.01%. The inconsistent velocity-pressure formulation is shown for illustrative purposes and is found to lose about 30% of the initial total energy and is thus highly dissipative. It must be eliminated on

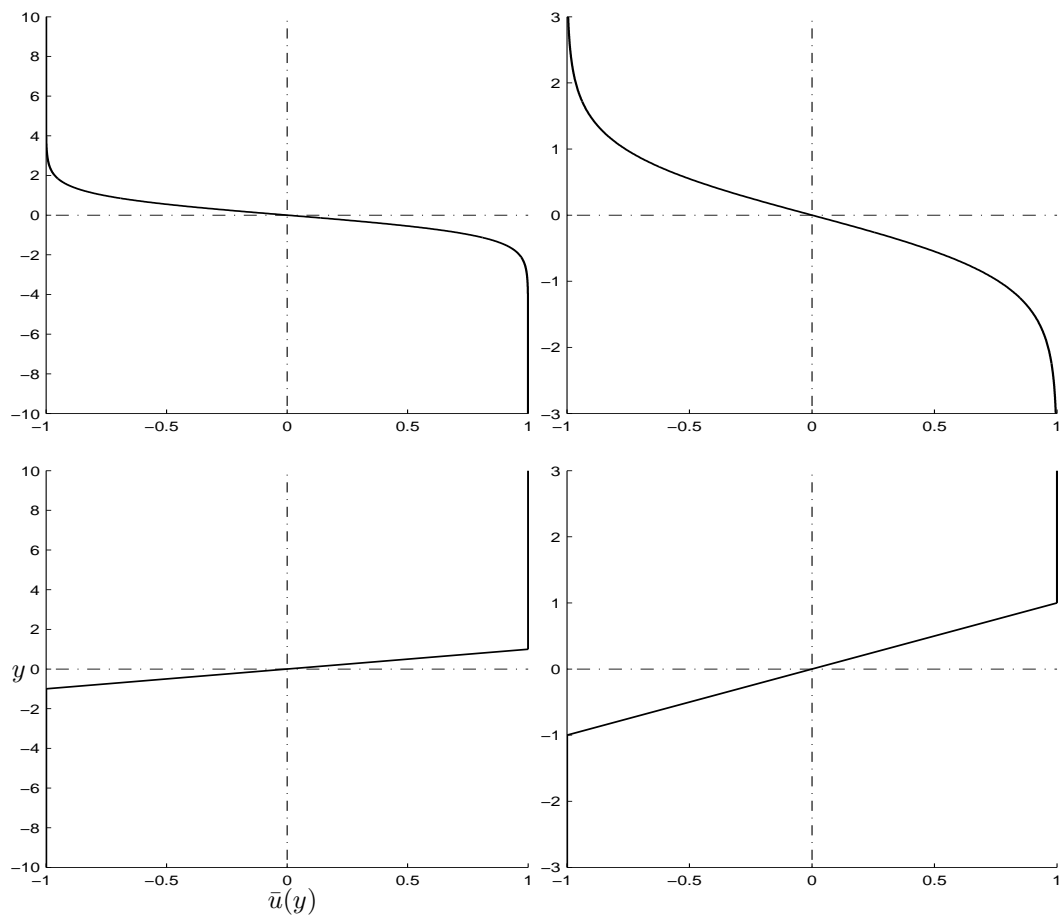


**Figure 2:** Top and bottom panels show the hyperbolic-tangent and piecewise linear basic shear flows, respectively. Panels on the right are blowups of those on the left, where focus is on the sheared zone.

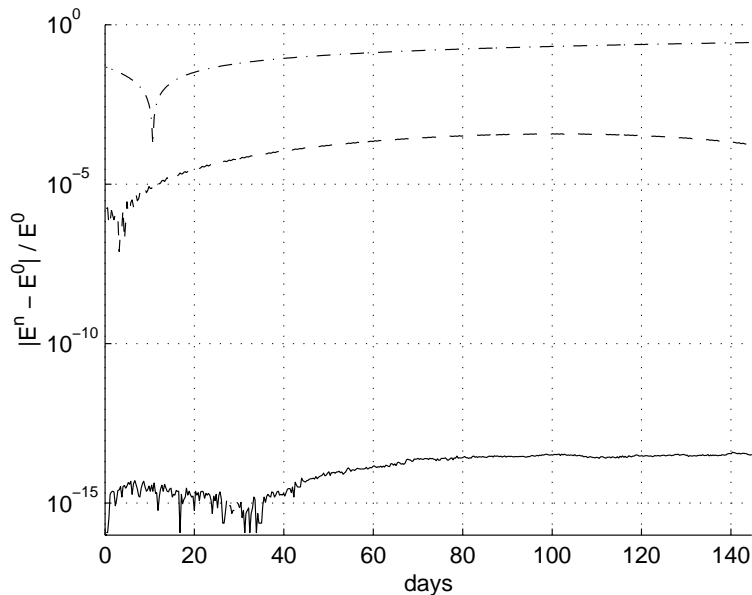


**Figure 3:** Relative energy deviation with respect to the total initial energy for the four formulations, starting with an unperturbed hyperbolic-tangent profile. Whereas the vorticity-stream function formulation exactly conserves energy (solid line), the deviation for the free-surface and consistent velocity-pressure formulations reaches about 0.01% (dashed line). The inconsistent velocity-pressure formulation sees its deviation attain an unacceptable level of 30% (dash-dotted line), and keeps increasing.

that ground. The fact that the free-surface and consistent velocity-pressure formulations are not as accurate as the vorticity-stream function formulation is caused by the explicit treatment of advective terms. It should be pointed out that, in all experiments aiming at evaluating growth rates, advection does not need any additional treatment to enhance the stability of the numerical scheme. This is so because advective terms remain small. Only when the nonlinear regime is investigated do we need to deal with streamline upwind weighting to ensure stability of the numerical scheme. In so doing, numerical dissipation is added to the flow. In what follows, wavenumbers  $\kappa$ , wavelengths  $\lambda$  and growth rates  $\delta$  are always dimensionless, unless otherwise specified.

### 5.1 The hyperbolic-tangent shear flow

The hyperbolic-tangent profile has been investigated by many authors in the past. For example, Michalke (1964) has determined the unstable eigenvalues on an  $f$ -plane ( $\beta = 0$ ) while Dickinson and Clare (1973) considered the  $\beta$ -plane system. All these studies are based on the rigid-lid, inviscid, equations (7)-(9) in an infinitely-wide, zonally periodic channel. Without delving into details – see Kuo (1973, 1978) instead –, we now give some key features. The hyperbolic-tangent velocity profile (37) is unstable to long waves, with a cutoff dimensionless wavenumber of  $\kappa = 1$  when  $\beta = 0$ . That is, the basic state will not grow unstable with a disturbance whose wavenumber exceeds  $\kappa = 1$ . On a  $\beta$ -plane, as  $\beta$  increases, the instability region narrows and for  $\beta > \frac{4}{3\sqrt{3}} = 0.7698$ , the flow is stable. The wavenumber of the most favored disturbance – i.e., the disturbance whose growth rate  $\delta$  is the largest – is 0.4449 when  $\beta = 0$  and shifts to higher values as  $\beta$  increases. On an  $f$ -plane, the dimensionless growth rate of the gravest mode is  $\delta = 0.188$ . On a  $\beta$ -plane, the growth rate of the most favored disturbance diminishes down to 0 as  $\beta$  increases.

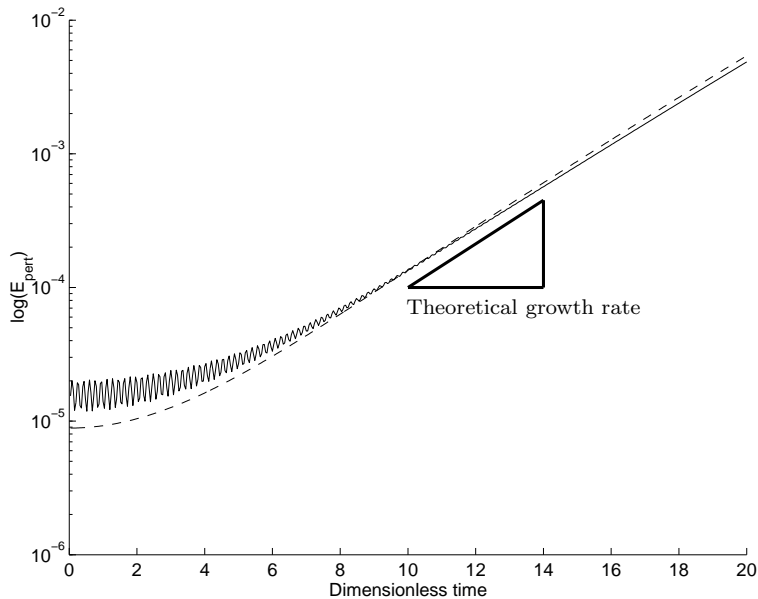


**Figure 4:** Evolution of perturbations kinetic energy for the vorticity-stream function (dashed line) and free-surface (solid line) formulations when the hyperbolic-tangent profile is perturbed with (39), where  $\kappa = 0.4$ . Note the presence of oscillations on the free-surface curve, caused by propagating truncation errors. The theoretical growth rate is that computed by Kuo (1978) for the vorticity-stream function formulation in an infinitely-wide channel.

When  $\beta = 0$ , instability may occur with disturbances characterized by wavenumbers ranging from 0 to 1. The basic state is disturbed with a wave of the form

$$\begin{cases} u' &= 0, \\ v' &= Ae^{-ry^2} \sin(\kappa x), \end{cases} \quad (39)$$

where  $A$  is the perturbation amplitude and  $\kappa$  is the wavenumber. The exponential function multiplying the sine wave confines the perturbation around  $y = 0$ . Wavenumbers ranging from 0.1 to 0.8, with an 0.1-increment, are chosen and, for each of them, the growth rate is determined by computing the perturbation kinetic energy. This procedure is repeated for each formulation, namely the vorticity-stream function, the velocity-pressure and the free-surface formulations. When the former is employed, the vorticity is to be perturbed. We do so by taking the *curl* of (39). The amplitude is taken to be one percent of the maximum value of the basic-state speed. Finally, the length of the numerical domain is  $L_x = n\lambda$ , where  $n$  is an integer and  $\lambda = 2\pi/\kappa$  is the wavelength to ensure that the perturbations be consistent with the periodic boundary conditions. In Figure (4), the evolution of perturbations kinetic energy is shown for the vorticity-stream function and the free-surface formulations when the hyperbolic-tangent profile is perturbed with (39), where  $\kappa = 0.4$ . A logarithmic  $y$ -scale emphasizes the exponential growth rate. The oscillations visible on the free-surface curve are spawned by the propagation of truncation errors. These are dominant until perturbations overcome them, which occurs around time 9.

To directly compare all three formulations, an initial hyperbolic-tangent velocity profile is prescribed, for which the shear layer occupies one tenth of the total domain width. The structured mesh used in this experiment and most subsequent ones is shown in Figure (8). It will be shown below that the same experiments carried out on meridionally extended meshes hardly alter the computed growth rates. Hence, a shear layer filling one tenth of the domain suffices to emulate the absence of northern and southern boundaries. This modeling aspect need not draw our attention as of now. The shear layer is resolved with about 6 elements. Results are

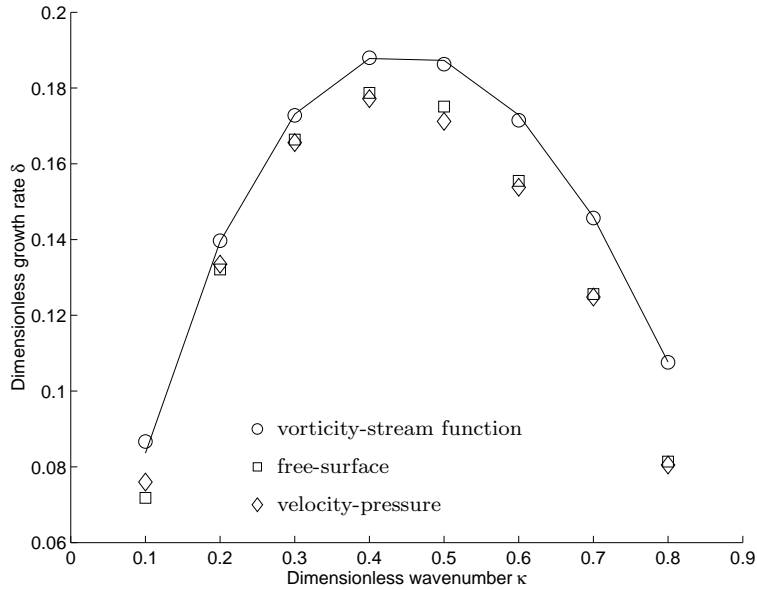


**Figure 5:** Growth rates for the three formulations on the same mesh resolving the shear layer with about 6 elements. The shear-layer width is a tenth of the domain width and the basic state is the hyperbolic-tangent profile. The solid line is the theoretical growth rate for the vorticity-stream function formulation.

shown in Figure (5), where it clearly appears that both the velocity-pressure and free-surface formulations yield growth rates that are smaller than that obtained with the vorticity-stream function formulation. The latter gives rise to growth rates that are very close to theoretical ones. The mean relative deviation amounts to less than 1 percent of theoretical growth rates while the mean relative deviation for the free-surface formulation is about 10 percent. The influence of the free surface and truncation errors can be further appraised by conducting the same experiment with the free-surface formulation on gradually-refined meshes. In particular, meshes resolving the shear layer with 5, 6 and 10 elements are employed and growth rates are reported in Figure (6). Convergence towards theoretical growth rates is achieved as resolution increases and we obtain mean relative deviations of 18, 10 and 5 percent, respectively. With increased resolution, truncation errors decrease and do not have as much ability of altering the linear unfolding of instabilities. Nonetheless, it should be kept in mind that, however high the resolution might be, the free-surface formulation remains intrinsically different from rigid-lid formulations and should not be expected to behave identically. The time derivative of the elevation is present and only can we hope to converge to theoretical growth rates in the limit of an infinite  $\alpha$ , multiplying the velocity divergence in the continuity equation (6).

As already mentioned, theoretical results are valid for infinitely-wide zonal channels but the numerical domain contains northern and southern boundaries. Those, however, should be located far enough from the shear layer so that their presence is hardly felt by the shear flow. An extended mesh is used to carry out the same experiments as those reported in Figure (5). That is, the shear-layer width remains the same but the meridional extent of the domain is three times that of the original domain. The domain extension uses a coarser resolution. In Figure (7), growth rates computed within the original and extended domains are reported for the vorticity-stream function and free-surface formulations. No significant difference can be brought to light between both domains. Thus, taking the shear-layer width to be one tenth of the computational domain width ensures that the boundaries have very little influence on the shear flow behavior. In our quest for the appraisal of the boundaries influence, a series of runs are now performed with shear flows contained within variable-width shear layers. Concretely, the shear-layer width

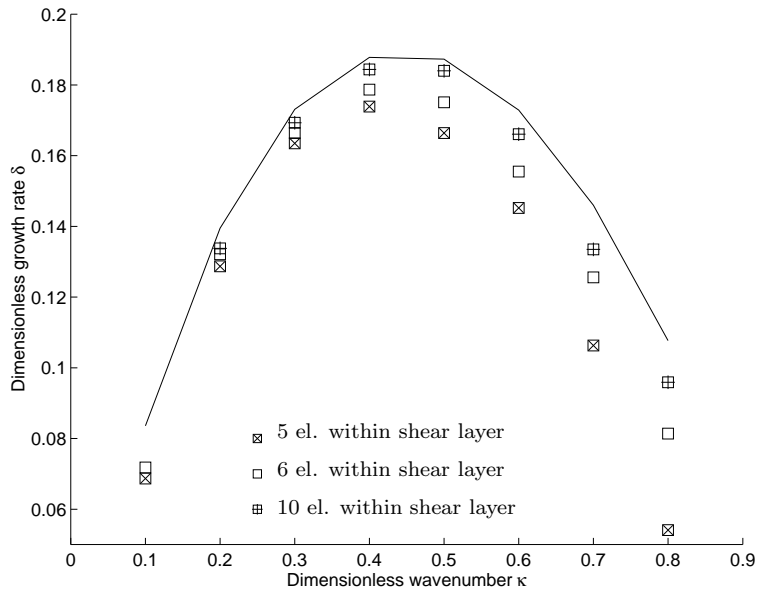


**Figure 6:** Growth rates for the free-surface formulation with gradually-refined meshes. In all experiments, the shear layer width is a tenth of that of the domain. As the mesh is refined, convergence towards theoretical growth rates is observed. Truncation errors associated with the initial basic state decrease with refinement. The value for  $\kappa = 0.1$  with the highest resolution is missing because the model grew numerically unstable (because of advection) before physical instabilities had time to develop.

increases while the computational domain remains unchanged. The vorticity-stream function formulation is employed for three different shear-layer widths: one tenth, one fifth and one third of the domain width. A shear-layer width of one third is depicted on the top right panel of Figure (2). As can be seen in Figure (9), the general trend is a decreasing computed growth rate for increasing shear-layer width. Because the boundaries get closer to the shear zone, instabilities are constrained and eddies do not unfold as freely. For a given shear-layer width, another trend is visible. For low wavenumbers (i.e., large wavelengths), the gap between computed and theoretical growth rates is the biggest. Because the length scale of instabilities eddies is on the order of the perturbation wavelength, should the latter increase, so would the size of eddies, which thus need more space to develop, unless boundaries hinder their unfolding.

Because unstructured meshes are inherent to the use of the finite element method, the experiment with the hyperbolic-tangent profile is repeated on the unstructured, non-uniform mesh shown in Figure (8), containing 8888 triangles, which is roughly the same number as in the structured mesh used to gather results of Figure (5). The shear-layer width is a tenth of that of the domain. Whereas growth rates obtained with the vorticity-stream function formulation remain fairly close to theoretical growth rates – as it should be –, a growing discrepancy is observed for the free-surface formulation for higher wavenumbers. The reason might be the following. As the basic flow is perturbed with wave disturbances of higher wavenumber (smaller wavelength), interferences between wave troughs and peaks are more likely to occur by propagating truncation errors, which, unlike for structured meshes, may do so in random directions. When this occurs, the perturbation wavenumber is not as definite and the basic flow is more likely to grow unstable with a mode that is closer to the gravest one.

## 5.2 The piecewise linear shear flow

We push further the idealization of the zonal flow by using the piecewise linear shear flow. As in the case of the hyperbolic-tangent shear flow, the domain is a periodic, infinitely wide zonal channel. As shown in Cushman-Roisin (1994), the dispersion relation for perturbations,

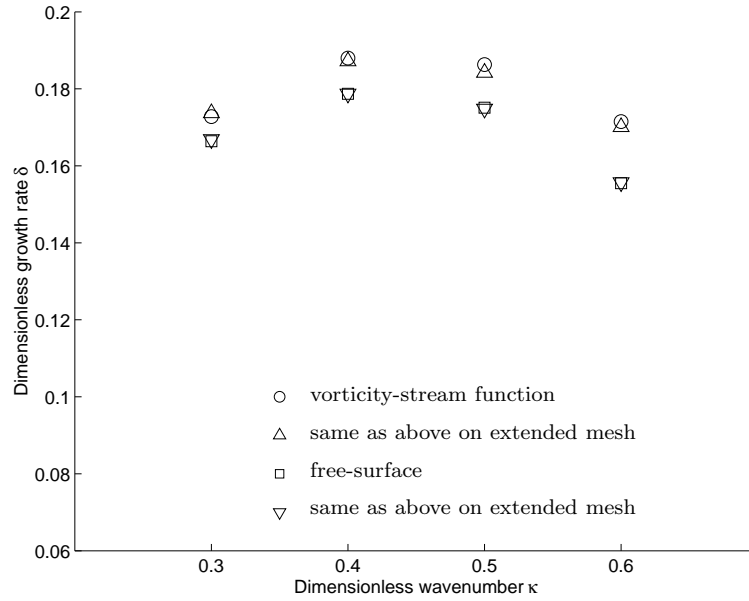


**Figure 7:** Experiments conducted on an extended mesh are compared with the same experiments conducted on the original mesh. No significant difference between the use of both domains can be reported. The shear-layer width is one tenth of the original domain width (hence 30 times thinner than the extended domain)

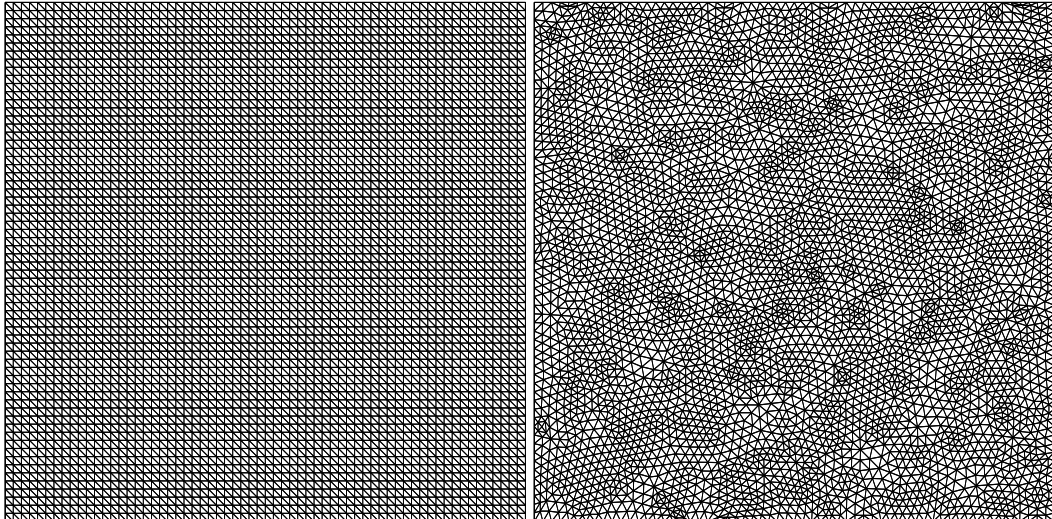


**Figure 8:** The structured mesh on the left contains 8192 triangles and the unstructured, non-uniform mesh on the right contains 8888 triangles. Note that the aspect ratio of length to width is 1:1 in the illustration but other aspect ratios are used for computations to ensure periodicity of perturbations (e.g.,  $\pi$ :1). In that case, anisotropic elements are used.

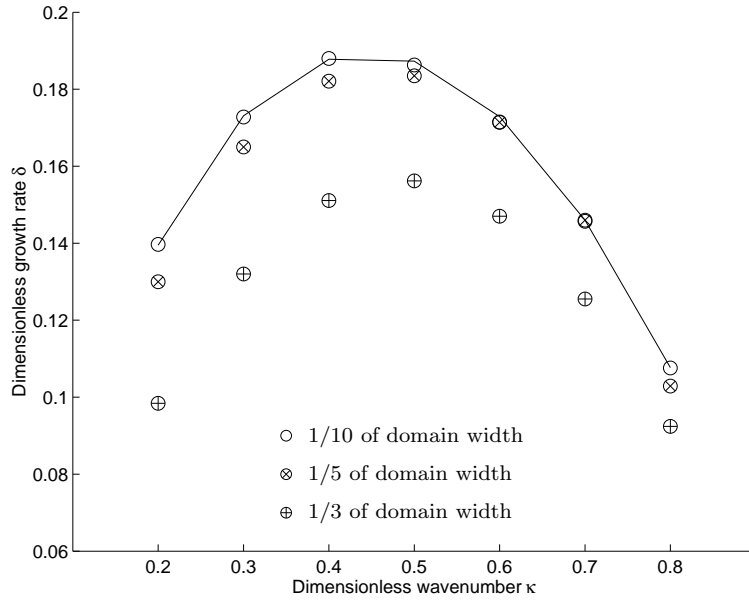


**Figure 9:** Growth rates computed with the vorticity-stream function formulation for varying shear-layer widths. As the width increases, growth rates decrease, due to the constraining presence of boundaries. Furthermore, for a given shear-layer width, the gap between growth rates of low-wavenumber perturbations and theoretical growth rates is the biggest. This translates the fact that large eddies do not unfold as freely.

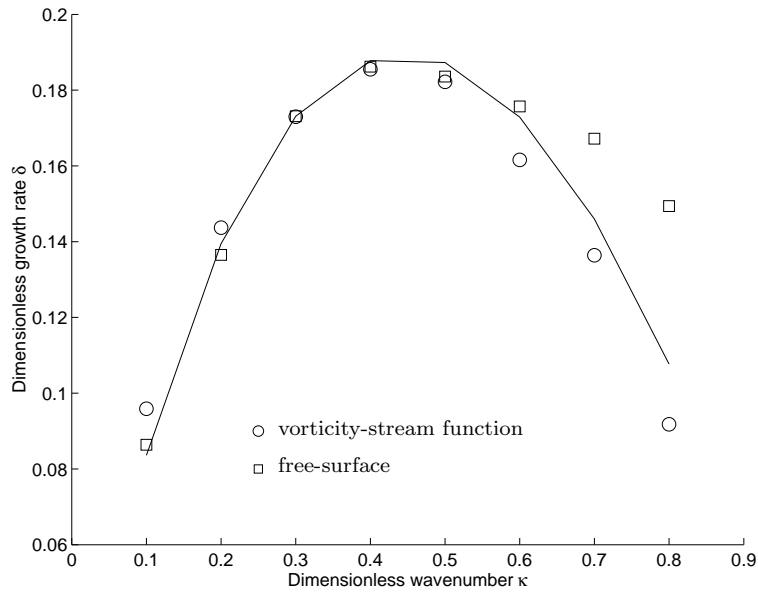


**Figure 10:** Growth rates for the free-surface and vorticity-stream function formulations on the unstructured mesh shown in Figure (8). The shear-layer width is a tenth of the total domain width and the basic state is the hyperbolic-tangent profile. The solid line is the theoretical growth rate for the vorticity-stream function formulation. Notice the overestimate obtained with the free-surface formulation for higher wavenumbers.

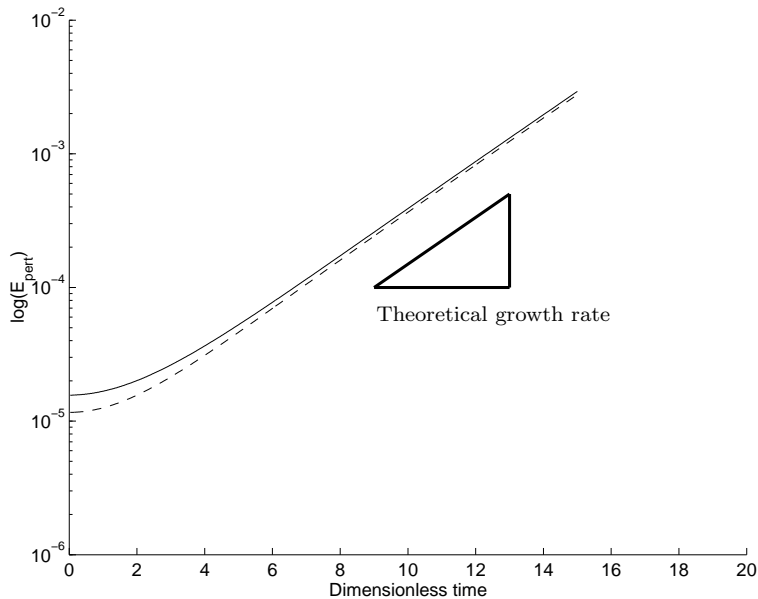


**Figure 11:** Evolution of perturbations kinetic energy for the vorticity-stream function (dashed line) and free-surface (solid line) formulations when the piecewise linear profile is perturbed with (39), where  $\kappa = 0.4$ . This should be compared with Figure (4) where oscillations made up the onset of the free-surface curve.

providing the wave velocity  $c$  in terms of the wavenumber  $\kappa$ , may be derived. The growth rate  $\delta = \kappa c$  is then given by

$$\delta(\kappa) = \frac{1}{2} [e^{-4\kappa} - (1 - 2\kappa)^2]^{1/2}.$$

Besides the possibility of deriving an analytical expression for the growth rate, the velocity is exactly interpolated with linear elements. A severe drawback of such a profile, though, is its lack of realism. However, the aim is here to be able to compare rigid-lid and free-surface formulations without having to deal with wavelike propagation of truncation errors. To illustrate this statement, the evolution of perturbations kinetic energy is shown in Figure (11), where the absence of oscillations at the onset of the free-surface curve is to be remarked. At this point, it must be stressed that, unlike the zonal velocity field and because the vorticity is discontinuous across the shear-layer frontiers, the vorticity cannot be interpolated exactly (unless the discontinuous finite element method is employed). This situation is depicted in Figure (12) and explained in detail in the caption.

In Figure (13), growth rates computed for all three formulations are shown and compared with the analytical results. The mesh resolves the shear layer with 5 elements (the meridional resolution is 20 km). The mean relative deviations are 4, 2 and 3 percent for the vorticity-stream function, free-surface and velocity-pressure formulations, respectively. Hence, none of them may significantly be categorized as yielding better results. The only trend, however, is a slight overestimate obtained when using the vorticity-stream function formulation. This might be due to the discontinuous nature of the initial vorticity field. A last experiment is carried out on a coarser mesh resolving the shear layer with 3 elements and having a meridional resolution of 50 km. Results are reported in Figure (14) and mean relative deviations are 8 and 6 percent for the free-surface and vorticity-stream function formulations, respectively. Because large-scale ocean models do not easily run on meshes with resolutions as high as 20 km (unless local refinement is implemented), the last experiment has been carried out to show that the use of a coarser mesh yields decent results.

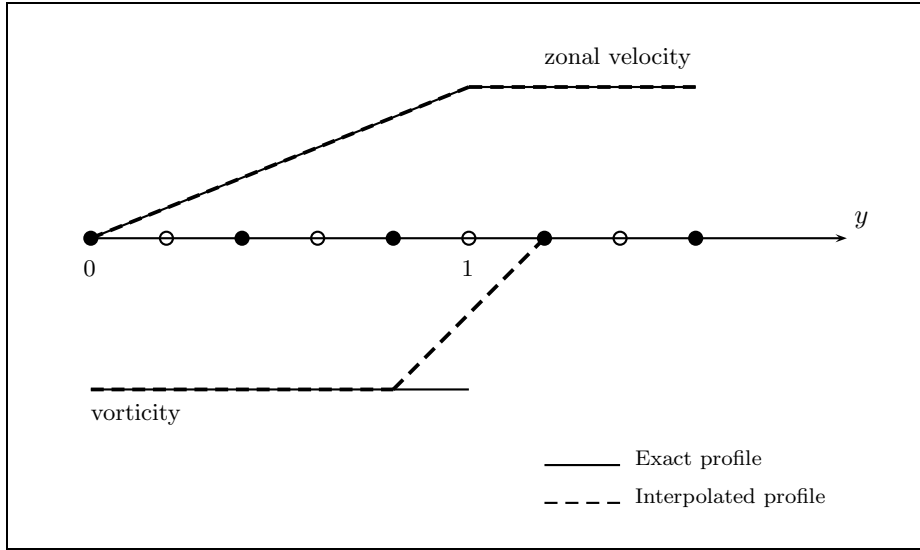


**Figure 12:** Since the zonal velocity is continuous, it is exactly interpolated with linear elements. On the other hand, the discontinuous vorticity cannot be interpolated and the discontinuity is, at best, linearly represented (see the dashed line). This leads to a poorer representation of the shear layer. The growth rate is directly proportional to the shear-layer width and it is unclear which length scale is to be used to compute the dimensionless growth rate when such an approximation prevails. Filled and empty circles represent vorticity and velocity nodes, respectively.

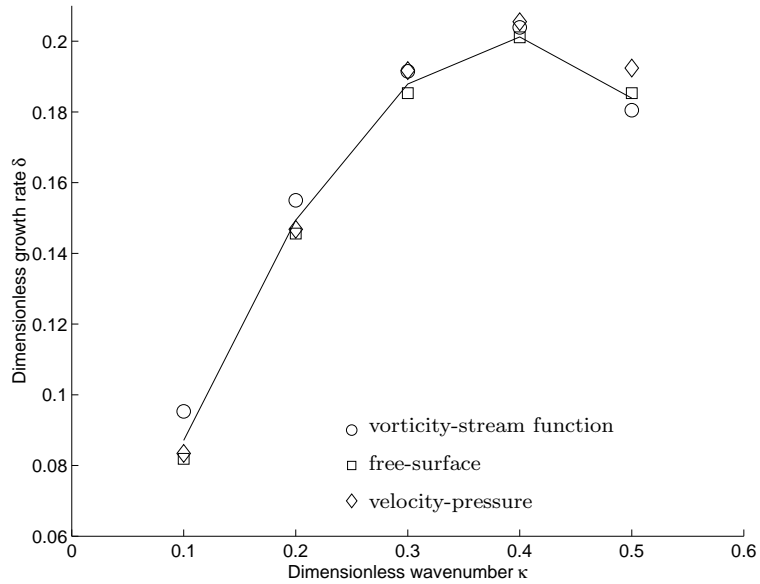


**Figure 13:** Growth rates for the three formulations on the same mesh resolving the shear layer with 5 elements (meridional resolution is 20 km). The shear-layer width is a tenth of the domain width and the basic state is the piecewise linear profile. The solid line is the theoretical growth rate for rigid-lid vorticity-stream function formulation.

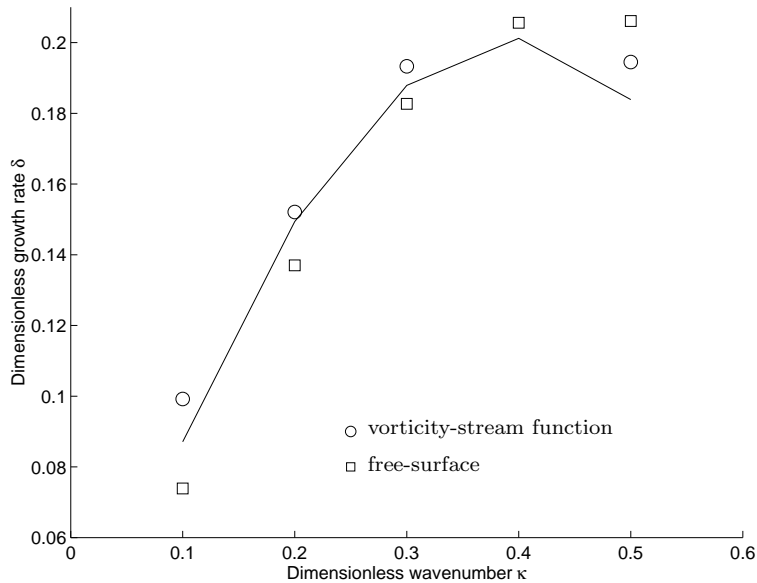


**Figure 14:** Growth rates for the vorticity-stream function and free-surface formulations on a coarse mesh resolving the shear layer with only 3 elements (meridional resolution is 50 km). The shear-layer width is 0.15 times the domain width (i.e., slightly wider than in previous experiments) and the basic state is the piecewise linear profile. The solid line is the theoretical growth rate for rigid-lid vorticity-stream function formulation.

### 5.3 The nonlinear regime

So far, all runs have been conducted over timescales that did not allow for nonlinear advective terms to become significant. Typical dimensionless run times were on the order of 20. That is, real run times of about 4 months. We now extend the dimensionless run time up to 100 (i.e., about 20 months). The phenomena that we witness in this case are not faithful representations of what could happen in the real ocean or atmosphere, because no physical process would have so much time to develop without interacting with external processes. Bearing that in mind, we now show the unfolding of eddies on two different meshes – the second one having its resolution doubled – for the vorticity-stream function and free-surface formulations. Nondimensionless time steps are 0.02 and 0.01, respectively. In both series of experiments, advection in the free-surface formulation is treated with full streamline upwind weighting, whereby numerical dissipation is added and without which the scheme would be unstable. In comparison, the vorticity-stream function formulation does not include any diffusion, be it physical or numerical. A striking difference between both formulations, as can be seen in Figures (15) and (16), is that eddies do not tend to merge in the free-surface formulation. Two additional features make up the free-surface formulation, as compared with the vorticity-stream function formulation. Those are the presence of the free surface and numerical dissipation. We could then wonder which factor (or combination of factors) leads to the inhibition of eddies unfolding. Even though, damping is most likely due to numerical dissipation, the role of the free surface cannot be ruled out altogether.

## 6 Conclusion

The principal goal of this work was to compare rigid-lid and free-surface finite-element models to represent barotropic instabilities. In particular, the principal goal was to appraise the influence of the free surface. For large-scale ocean modeling, the time derivative of the sea surface elevation appearing in the continuity equation (6) is at least two orders of magnitude smaller

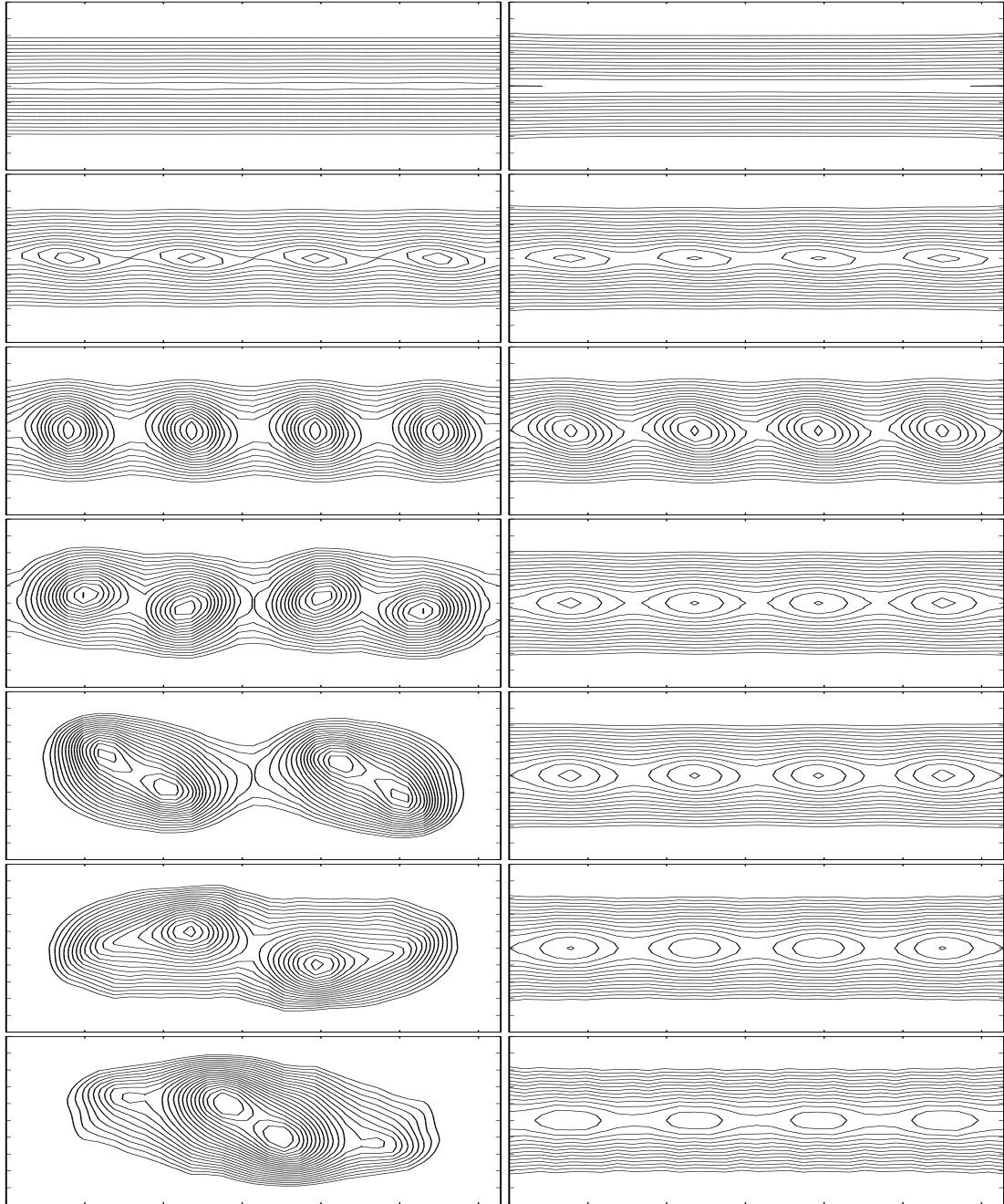


**Figure 15:** Comparison between the vorticity-stream function (left panels) and free-surface (right panels) formulations in the nonlinear regime on an intermediate-resolution mesh (meridional resolution of 31 km). The stream function is shown. Dimensionless snapshot times are 0, 20, 30, 60, 70, 90 and 100. Distances between two  $x$ -tics and two  $y$ -tics are 500 km and 100 km, respectively. The time step is 0.02. The basic state is the piecewise linear profile.

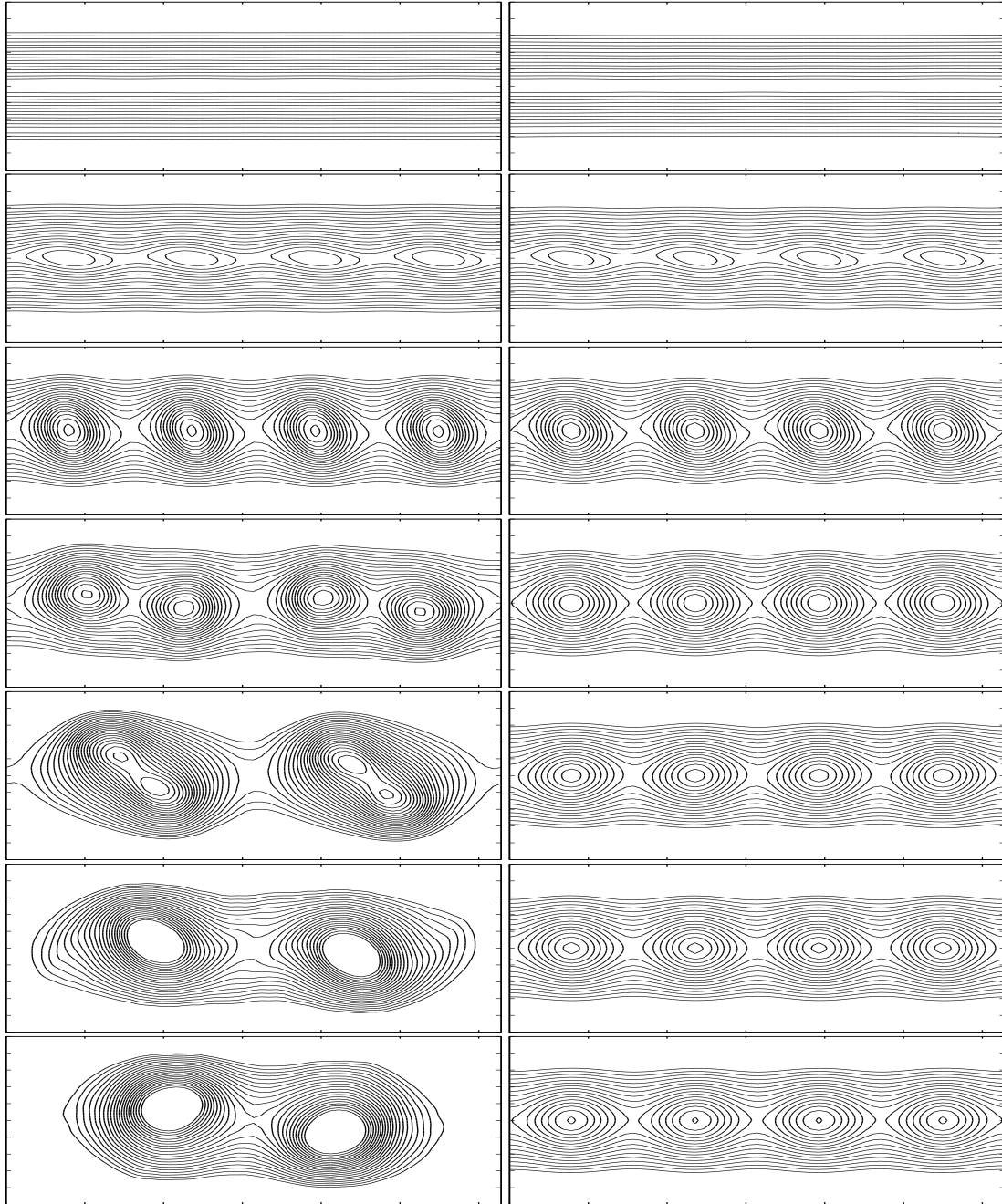


**Figure 16:** Comparison between the vorticity-stream function (left panels) and free-surface (right panels) formulations in the nonlinear regime on a fine mesh (meridional resolution of 15 km). The mesh resolution is twice that used in Figure (15). The stream function is shown. Dimensionless snapshot times are 0, 20, 30, 60, 70, 90 and 100. Distances between two  $x$ -tics and two  $y$ -tics are 500 km and 100 km, respectively. The time step is 0.01. The basic state is the piecewise linear profile.

than the velocity divergence, hence a priori justifying the rigid-lid assumption. Therefore, any differences in the growth rates were expected to be small. Two series of experiments were conducted to assess the role of the free surface and both were aimed at computing growth rates and comparing them to theoretical solutions valid for the vorticity-stream function formulation. In the first series, the hyperbolic-tangent profile was used and it was shown that the free-surface formulation yielded growth rates that converged to theoretical ones as the mesh was refined. For coarser meshes, initial truncation errors are fairly important and are allowed to propagate as surface waves. Growth rates thus computed were smaller than theoretical ones and more so for low-resolution meshes. It is believed that propagation of truncation errors as surface waves allows for energy to be redistributed and carried away from within the shear flow towards the boundaries. The velocity-pressure formulation yielded results that were roughly identical to that of the free-surface formulation. The surface pressure merely plays the role of elevation by providing enough pressure to keep the sea surface flat. This formulation thus allows for pressure waves to propagate.

Because theoretical results were derived for infinitely-wide channels, it was important to carry out a sensitivity analysis with respect to the location of boundaries. The original computational domain was ten times wider than the shear-layer width (an aspect ratio of 1/10). Growth rates were then computed for increasing aspect ratios. The vorticity-stream function was utilized to perform this analysis. The general trend is a decreasing growth rate for an increasing aspect ratio, for eddies development is hindered by the presence of boundaries. The decrease in growth rate is sharper for low-wavenumber instabilities. The latter are characterized by larger eddies (whose diameter is on the order of the wavelength) that need minimal meridional extension to unfold. Finally, an experiment using a mesh having an aspect ratio of 1/30, with coarser southern and northern mesh extensions, was shown to yield the same results as that obtained with the original mesh.

In order to do away with this issue of truncation errors, a piecewise linear profile was then used. Although velocity was exactly interpolated with linear elements, the discontinuous vorticity could not be so. This permitted to concentrate on the free surface, not as a carrier of truncation errors but as a variable per se. On a moderate-resolution mesh (meridional resolution of 20 km), all three formulation gave rise to growth rates close to theoretical ones and, most importantly, no one furnished results that could have allowed us to choose it as the right one.

All experiments were carried out with  $\alpha = 27$ . In order to have a grasp on the role of the free surface, one should work with  $\alpha$  close to 1. However, only two parameters may vary: the layer depth  $h$  and the shear-layer length scale  $L$ . To achieve a value of 1, those two parameters have to assume values that would either break down the assumptions underlying the model upon which theoretical results are drawn, or render the domain unphysical. Decreasing  $h$  down to a few tens of meters while keeping the domain width at 1000 km is certainly numerically feasible but would produce unapplicable results. At the other end of the spectrum, increasing the shear-layer width by a factor of 10 implies having a domain width of ten thousand kilometers, whereupon the  $\beta$ -plane approximation does not hold any more.

Nonlinear effects were then examined by extending the run time up to 100, that is, 10 times longer than in all previous runs. While merging of eddies characterize the solution for the vorticity-stream function formulation, their unfolding seems to be inhibited by numerical dissipation in the free-surface formulation. The latter treats advection with streamline upwind weighting, which stabilizes the scheme, yet prevents instabilities to grow. This brings up an important aspect of ocean modeling, whereby numerical stability is always sought but should in now way overdissipate physical processes. On the other hand, the vorticity-stream function formulation, which allows for an inverse energy cascade to exist, is devoid of dissipation of any kind and, as such, does not comply with reality either.

## Acknowledgements

Laurent White and Eric Deleersnijder are a Research fellow and a Research associate, respectively, with the Belgian National Fund for Scientific Research (FNRS). The present study was

carried out within the scope of the project “A second-generation model of the ocean system”, which is funded by the *Communauté Française de Belgique*, as *Actions de Recherche Concertées*, under contract ARC 04/09-316. This work is a contribution to the construction of SLIM, the Second-Generation Louvain-la-Neuve Ice-ocean Model. The authors are indebted to Benoit Cushman-Roisin for the comments he provided during the first stages of the preparation of this paper.

## References

- Beckers, J.-M., and Deleersnijder, E., 1993. Stability of a FBTC scheme applied to the propagation of shallow-water inertia-gravity waves on various space grids. *Journal of Computational Physics*, **108**(1), 95-104.
- Cushman-Roisin, B., 1994: Geophysical Fluid Dynamics. Prentice Hall, Upper Saddle River, NJ.
- Dickinson, R. E., and Clare, F. J., 1973: Numerical study of the unstable modes of a hyperbolic-tangent barotropic shear flow. *Journal of the Atmospheric Sciences*, **30**, 1035-1049.
- Gresho, P. M., Chan, S. T., Lee, R. L., Upson, C. D., 1984: A modified finite element method for solving the time-dependent, incompressible Navier-Stokes equations. Part 1: theory. *International Journal for Numerical Methods in Fluids*, **4**, 557-598.
- Gresho, P. M., and Sani, R. L., 1987: On pressure boundary conditions for the incompressible Navier-Stokes equations. *International Journal for Numerical Methods in Fluids*, **7**, 1111-1145.
- Gresho, P. M., and Sani, R. L., 1998: Incompressible flow and the finite element method. John Wiley and Sons.
- Hanert, E., Le Roux, D. Y., Legat, V., Deleersnijder, E., 2004: Advection schemes for unstructured grid ocean modelling. *Ocean Modelling*, **7**, 39-58.
- Hanert, E., Le Roux, D. Y., Legat, V., Deleersnijder, E., 2005: An efficient Eulerian finite element method for the shallow water equations. *Ocean Modelling*, **10**, 115-136.
- Hart, J. E., 1974: On the mixed stability problem for quasi-geostrophic ocean currents. *Journal of Physical Oceanography*, **4**, 349-356.
- Hua, B., and Thomasset, F., 1984: A noise-free finite element scheme for the two-layer shallow water equations. *Tellus*, **36A**, 157-165.
- Killworth, P. D., 1980: Barotropic and baroclinic instability in rotating stratified fluids. *Dynamics of Atmospheres and Oceans*, **4**, 143-184.
- Kuo, H. L., 1949: Dynamic instability of two-dimensional non-divergent flow in a barotropic atmosphere. *Journal of Meteorology*, **6**, 105-122.
- Kuo, H. L., 1973: Dynamics of quasigeostrophic flows and instability theory. *Advances in Applied Mechanics*, **13**, 247-330.
- Kuo, H. L., 1978: A two-layer model study of the combined barotropic and baroclinic instability in the tropics. *Journal of the Atmospheric Sciences*, **35**, 1840-1860.
- Michalke, A., 1964: On the inviscid instability of the hyperbolic-tangent velocity profile. *Journal of Fluid Mechanics*, **19**, 543-556.
- Pedlosky, J., 1964: The stability of currents in the atmosphere and the ocean: Part I. *Journal of the Atmospheric Sciences*, **2**, 201-219.
- Pedlosky, J., 1979: Geophysical fluid dynamics. Springer-Verlag.
- White, L., Legat, V., Deleersnijder, E., and Le Roux: A one-dimensional benchmark for the propagation of Poincaré waves. *Submitted to Ocean Modelling*, December 2004.